Michalowski Radoslaw L. (Orcid ID: 0000-0002-9557-4802)

Intricacies in three-dimensional limit analysis of earth slopes

Dowon Park[1] and Radoslaw L. Michalowski[1,2]

Summary

Analyses of three-dimensional slope failures can be elaborate because of the complexity owed to the geometry of the failure mechanism that needs to conform to an admissible kinematics of the slope collapse. This admissibility is imposed by the soil limit state condition, the normality plastic flow rule, and the boundary conditions. The kinematic approach of limit analysis is employed, and a rotational 3D slope failure is revisited. The study leads to the conclusion that some geometric constraints used in previous studies limit the range of admissible mechanisms resulting in overestimating stability factors. A set of results is presented that was obtained using an algorithm that allowed eliminating limitations present in previous studies. The largest improvements in the solutions were found for undrained failures of narrow slopes. For a 30° slope limited in width by the width-to-height ratio of 0.6, the stability factor calculated in previous studies overestimated the current calculations by nearly 39%. This overestimation is smaller for drained failures and it drops significantly with an increase in the width of the failure mechanism.

Key Words: Landslides, Slope stability, Limit analysis, Plasticity analysis

1. INTRODUCTION

Safety assessment of slopes is an important exercise in geomechanics. Typical stability analyses involve two-dimensional considerations, but in many cases a three-dimensional analysis is called

[1] Department of Civil & Environmental Eng., University of Michigan, Ann Arbor
[2] Corresponding author, 2028 G.G. Brown Bldg, AnnArbor, MI 48109-2125; e-mail: rlmich@umich.edu, tel: (734) 763-2146, fax: (734) 764-4292.

for. For example, excavation slopes or soil slopes limited in width by a rock outcrop require three-dimensional analyses if an accurate assessment is needed.

Observations of failure surfaces in clays were documented as early as 1846 by Collin[1], but 2D analyses of stability were not introduced until the 20th Century (Fellenius[2], Taylor[3], Drucker and Prager[4]). Three-dimensional analyses of stability of slopes can be grouped into traditional limit equilibrium methods, limit analysis, and numerical approaches such as finite element analysis. The 3D analyses were first developed for undrained failures, as the mechanisms in incompressible materials are easier to construct (Baligh and Azzouz[5], Gens et al.[6]). The early 3D analyses for pressure-dependent materials were based on traditional limit-equilibrium slice methods extended to 3D failures[7,8,9]. Drescher[10] presented a one-block collapse mechanism in a pressure-dependent material, while a 3D multi-block limit analysis was presented by Michalowski[11]. Leshchinsky et al.[12] developed a rotational mechanism in pressure-dependent materials using a limit equilibrium approach, with a kinematically admissible mechanism arrived at through a variational approach. The outcome of that approach was equivalent to kinematic limit analysis. A rotational mechanism was also considered by De Buhan and Garnier [13]. A 3D rotational mechanism was postulated by Michalowski and Drescher[14], which was used in a series of related publications[15, 16, 17, 18]. More recently, the variational approach to finding the critical failure surface was revisited by Zhang et al.[19]. While purely rotational mechanisms may not necessarily be the most critical[20], the rotational collapse appears to be more critical than other 3D mechanisms suggested throughout the literature.

Finite element analysis of two- and three-dimensional slope failures was considered throughout the literature[21,22,23,24], while the finite element implementation of limit analysis for the purpose of safety assessment of slopes (3D) was also presented in recent years[25,26]. Numerical approaches have advantages of accounting for soil inhomogeneities and not having to predetermine the mode of failure. However, when it comes to assessment of stability, they also come with some

disadvantages. For example, at the time of stability loss, the solution does not converge in the finite element analyses, and a lack of convergence in a prescribed number of iterations is often considered as a criterion for reaching instability. This is not an elegant procedure, though it has proved to be effective. An advantage of using finite element implementation of limit analysis is in its ability to find both the upper and lower bounds to the true solution, whereas the more common "analytical" method can be used effectively only with the kinematic approach of limit analysis. It is not uncommon, however, that a well-chosen mechanism in the analytical approach can yield a better solution to a stability measure than the finite element approach[15,19,27].

The slope failure mechanism considered in this paper can be applied to slopes with arbitrary limitations on the slope width. Failing mass in natural slopes, particularly hillside slopes, is often constrained by bedrock[22,23], while the kinematics can also be affected by a rock outcrop and the terrain topography[28]. These kinematic constraints are not considered in this paper, although the limitation on the depth of the mechanism can be easily introduced into the analysis by placing a proper constraint on the optimization process.

This paper's focus is on the kinematic approach of limit analysis in slope stability considerations. In particular, the rotational failure mechanism is revisited to assess the source of differences in the outcomes of analyses coming from different studies, but based on the same mechanism of failure. The kinematic approach is described briefly first, followed by the description of the 3D collapse mechanism and the geometric intricacies in the mechanism that are likely to be the source of discrepancies in the results published throughout the literature.

2. KINEMATIC LIMIT ANALYSIS APPLIED TO SLOPES

2.1. *Material model and limitations of the method*

Limit analysis has been widely applied in stability of structures and plastic forming of metals (Hill[29]), followed by applications in geotechnical engineering (Drucker and Prager[4], Salençon[30],

Chen[31]). The fundamental assumption in the analysis is the perfectly plastic behavior of the material, described by a convex yield condition and the normality plastic flow rule. This assumption allows using the postulate of maximum plastic work, which, in turn, allows proving the theorems of limit analysis. The yield criteria for metals are pressure-independent, and the outcome of application of the normality flow rule is incompressible plastic flow, which is consistent with experimental observations for metals. With yielding of geomaterials exhibiting pressure dependency, the associative (normality) flow rule leads to dilative plastic deformation, typically overestimating the observed volumetric strains. Application of the non-associative flow rule to geomaterials was considered early by Mróz[32].

Plastic deformation of geomaterials does not conform to the normality flow rule (typically, normality law overestimates volumetric deformation), and the reason for using associativity in limit analysis is purely mathematical: without the normality flow rule, the theorems of limit analysis cannot be proved. Hence, the associativity of plastic flow is needed for the solutions to boundary value problems to be strict lower or upper bounds to a true solution. The kinematic approach is used in this paper, and we refer to the theorem used as the *kinematic theorem of limit analysis*. This theorem is more commonly referred to as the *upper-bound theorem*, but this term is ambiguous. This is because the outcome of application of this theorem can be either an upper bound, for instance, when the active limit load is calculated, or a lower bound when a passive force (reaction) is sought. Whether the material obeys associativity or not, it can be proved that this approach yields a rigorous bound to the true solution. This was shown by Redenkovic[33] and, with an intuitive graphical interpretation, by Palmer[34]. For this very same reason, the normality-sliding rule was used in problems with frictional boundary conditions, where the true sliding rule made the analytical solution not possible (Collins[35], Mróz and Drescher[36], Michalowski and Mróz[37]).

Limit analysis is an approximate method, but it yields a rigorous bound to the true solution. However, not every stability problem can be addressed with limit analysis. This is because the theorems of limit analysis, strictly, only allow calculations of a bound on an integral of the rate of work of the unknown load, and not every boundary condition allows extracting the load from this integral. For instance, a limit force on a footing can be found using limit analysis if the boundary condition is given as a rigid translation of the footing, but if the kinematic boundary condition is given in terms of rotation, one can only find a limit moment, but not the force. This is one of the limitations of the method. Another limitation follows from the integral form of the work rate balance, making it possible to find limit forces (or moments), but not their distributions. The stress field cannot be determined either. Finally, only incipient stability problems can be tackled, and no displacements or progressive failure can be tracked with confidence. The formulation of the slope stability problem involves a static boundary condition, most typically a stress-free boundary.

2.2. *Equilibrium in kinematic limit analysis*

The common form of the work rate balance equation used in the kinematic approach can be written as

$$\int_V \sigma_{ij}\dot{\varepsilon}_{ij}^{pl}\,dV + \int_L T_i\,[v]_i\,dL = \int_S T_i v_i\,dS + \int_V X_i v_i\,dV \qquad (1)$$

where the two terms on the left-hand side represent the rate of plastic work dissipation (internal work), and the two terms on the right-hand side depict the rate of external work (see Notation for explanation of symbols). The first term on the left-hand side represents the work dissipation rate in volume V (due to plastic strain within the volume), and the second one is the dissipation on kinematic discontinuity surfaces L. The first term on the right-hand side represents the work rate of traction vector T_i on boundary S of the mechanism, and the second term is the work rate of distributed forces X_i in volume V (e.g., gravity load). The kinematic theorem indicates that the left-hand side (the rate of plastic work) is not smaller than the work rate of the true external loads

(right-hand side) in any kinematically admissible mechanism of plastic deformation. Manipulation of Eq. (1) allows one to find a rigorous bound on an unknown limit load. For example, in the case of a footing on boundary S, one could find an upper bound to the footing limit load (integral of traction T_i on boundary S), if the velocity on this boundary, v_i, was constant (rigid translation). However, the left-hand side of the balance in Eq. (1) is calculated based solely on the yield condition and normality flow rule applied to the postulated failure mechanism; hence, in general, stress field σ_{ij} does not satisfy equilibrium. Therefore, Eq. (1) cannot be considered the principle of virtual work for a deformable body. For a rigid-body translational mechanism, however, the first term in Eq. (1) is zero, and the remaining terms assume the form of the principle of virtual work for a rigid-body mechanism. Consequently, the equilibrium of forces (not stresses) will be enforced if Eq. (1) is used to calculate an unknown force in a rigid block mechanism. This was shown explicitly by Michalowski[11] (see also Drescher and Detournay[38] and Salençon[39]). Similarly, global equilibrium of moments will be enforced in a rigid rotational mechanism.

3. ROTATIONAL 3D FAILURE MECHANISM

There are relatively few limit analysis solutions to slope stability that include three-dimensional mechanisms of failure in pressure-dependent materials. The early ones are the translational mechanisms, including the classical wedge-type failure often exploited in rock mechanics with a limit equilibrium type of solution[40], a single-block mechanism by Drescher[10], and a multi-block mechanism by Michalowski[11]. A rotational mechanism of slope failure was used in limit analysis by De Buhan and Garnier[13] and by Michalowski and Drescher[14]. A special case of the mechanism postulated by Michalowski and Drescher[14] was arrived at earlier by Leshchinsky et al.[12], and it was exploited further more recently by Zhang et al.[19]. The primary method used by Leshchinsky et al.[12] was the limit equilibrium method with the variational approach used to optimize the mechanism of failure. The kinematics in these rotational mechanisms is plane, but the geometry of the failure surface is three-dimensional.

3.1. *Curvilinear cone failure surface*

A curvilinear cone failure surface was postulated in Michalowski and Drescher[14] by requiring that all radial cross sections of the cone are circles, and the trace of the cone on the plane of symmetry is governed by two log-spirals

$$r(\theta) = r_0 \, e^{(\theta-\theta_0)\tan\phi} \tag{2}$$

$$r'(\theta) = r_0' \, e^{-(\theta-\theta_0)\tan\phi} \tag{3}$$

with r_0 and r_0' illustrated in Fig. 1. Effectively, this surface is generated by revolving a circle of variable radius $R(\theta)$

$$R(\theta) = \frac{r(\theta) - r'(\theta)}{2} \tag{4}$$

about an axis passing through center O. The central line of the generated curvilinear cone is described by radius $r_c(\theta)$

$$r_c(\theta) = \frac{r(\theta) + r'(\theta)}{2} \tag{5}$$

With the material strength described by the Mohr-Coulomb criterion, such a surface forms an admissible failure surface in the rotational mechanism as it assures that the vector of velocity is inclined at internal friction angle ϕ to the conical surface at every point of the surface. Such surface was earlier postulated in a translational mechanism under square and rectangular footings[41], and was more recently used to analyze passive pressure on retaining walls[42]. This surface can also be modified to account for pressure-dependent geomaterials with non-linear strength envelopes[43,44]. Since its inception, the 3D slope failure mechanism postulated[14] was adopted in many slope stability studies. The mathematical description of this mechanism is

redeveloped here to remove some of the restrictions, and to allow for finding more critical failure surfaces. This new and more general algorithm is also simpler than the one originally presented[14].

In the polar co-ordinate system ρ,θ the contour of the slope can be described as a piece-wise linear function $r_s(\theta)$ (see Fig. 1)

$$r_s(\theta)=\begin{cases}\dfrac{r_0\sin\theta_0}{\sin\theta}, & \theta_0<\theta\le\theta_B\\ \dfrac{r_h\sin(\beta+\theta_h)}{\sin(\beta+\theta)}, & \theta_B<\theta\le\theta_C \quad (\theta_C=\theta_h \text{ for toe failure})\\ \dfrac{r_h\sin\theta_h}{\sin\theta}, & \theta_C<\theta\le\theta_h \quad \text{(Below-toe only)}\end{cases} \tag{6}$$

where

$$r_h = r_0 e^{(\theta_h-\theta_0)\tan\phi} \tag{7}$$

and

$$\theta_B = \arctan\left(\frac{r_h\sin\theta_h - H}{r_h\cos\theta_h + H\cot\beta}\right) \tag{8}$$

and θ_0, θ_h, and θ_C are independent geometrical parameters ($\theta_C = \theta_h$ for toe failures). The mechanism in Fig. 1 differs from that in Michalowski and Drescher[14] in the following detail: the center line $r_c(\theta)$ of the curvilinear cone intersects the slope ($r_c > r_s$, see Eqs. (5) and (6) for r_c and r_s), whereas in the former the surface was limited to cases where its center line (Eq. (5)) could be tangent to the slope surface, but could not intersect the slope. This limitation was implied by an intuitive conjecture that a critical mechanism will not have "overhanging" regions in the stationary portion of the slope. However, it was found that for some combinations of slope geometry and material properties, the most critical mechanism is one where the center line of the

cone intersects the slope ($r_c > r_s$), as indicated in the upper portion of the slope in Fig. 1. If an undrained failure is considered, the shape of the failure surface in Fig. 1 becomes a torus.

The slope has a stress-free boundary, and the collapsing block rotates as a rigid body, hence there are only two non-zero terms in Eq. (1): the rate of work dissipation D along the failure surface and the rate of work of the soil weight W_γ

$$\int_L T_i [v]_i \, dL = \int_V X_i v_i \, dV \tag{9}$$

or

$$D = W_\gamma \tag{10}$$

We first derive an expression for term W_γ. A new algorithm is developed for calculating W_γ in order to include cases with $r_c > r_s$. A general expression can be written as

$$W_\gamma = \int_V \gamma v \cos\theta \, dV \tag{11}$$

where γ is the soil unit weight, v is the velocity magnitude, θ is the angle between the velocity and the gravity direction, and V is the volume of the rotating block. The infinitesimal volume element shown in Fig. 1 (hatched stripe) is calculated as

$$dV = \rho \sqrt{R^2 - (\rho - r_c)^2} \, d\rho \, d\theta \tag{12}$$

With velocity magnitude v given by $v = \omega\rho$ (ω - angular velocity about axis through point O) and its direction perpendicular to ρ, one obtains

$$W_\gamma = 2\omega\gamma \int_{\theta_0}^{\theta_h} \int_{r_s}^{r} \rho^2 \cos\theta \sqrt{R^2 - (\rho - r_c)^2} \, d\rho \, d\theta \tag{13}$$

where the lower and upper radial integration limits r_s and r are defined in Eqs. (6) and (2), respectively. A general expression for the rate of work dissipation along a failure surface can be written as

$$D = \int_S c\, v \cos\phi \, dS \tag{14}$$

where c is cohesion, ϕ is the internal friction angle and S is the area of the failure surface. With the infinitesimal surface element dS (Fig. 1)

$$dS = dl\, da = \frac{\rho}{\cos\phi} \frac{R}{\sqrt{R^2 - (\rho - r_c)^2}} d\rho\, d\theta \tag{15}$$

the rate of work dissipation can be calculated as

$$D = 2c\omega \int_{\theta_0}^{\theta_h} \int_{r_s}^{r} \rho^2 \frac{R}{\sqrt{R^2 - \left(\rho - r_c\right)^2}} d\rho d\theta \tag{16}$$

where the lower and upper radial limits r_s and r are defined in Eqs. (6) and (2), respectively. Substituting the expressions in Eqs. (13) and (16) into Eq. (10), one can determine the upper bound to the stability factor defined as

$$N_f = \frac{\gamma H}{c} \tag{17}$$

or a lower bound to its reciprocal, often referred to as the stability number[3]

$$N_n = \frac{1}{N_f} = \frac{c}{\gamma H} \tag{18}$$

The best solution is found through minimization of N_f with angles θ_0, θ_C, θ_h, and ratio r_0' / r_0 being variable. If ratio r_0' / r_0 is restricted to $r_0' / r_0 \geq 0$, the critical mechanism has a finite

width, with the critical solution typically when $r_0'/r_0 = 0$. However, it is counterintuitive that a 3D solution would not approach the 2D solution in the absence of any restriction on the width of the failure. The cause of this peculiarity is presumably in that the curvature of the failure surface in the central cross-section (Fig. 1) is not independent of the curvature in the cross-section perpendicular to the plane of Fig. 1. To remove this limitation, an alternative mechanism was developed (Michalowski and Drescher[14]), where negative ratio r_0'/r_0 was allowed. The respective mechanism is illustrated in Fig. 2. The log-spiral in Eq. (3) is now replaced with

$$r'(\theta) = -r_0' e^{(\theta-\theta_0)\tan\phi} \tag{19}$$

With ratio r_0'/r_0 dropping to large negative numbers, the size of the circular cross-section (shaded area in Fig. 2(a)) increases (curvature decreases), whereas the curvature in the plane of symmetry is not coupled with this change. Consequently, the solution to the stability factor approaches an asymptote with a decrease in ratio r_0'/r_0, but this asymptotic solution is not equal to the 2D solution. For example, for a 45-degree slope and $\phi = 15°$, the asymptotic solution is about $\gamma H/c = 14.11$, whereas the 2D solution is $\gamma H/c = 12.05$.

Based on a different premise (limit equilibrium and variational approach to finding the critical solution), Leshchinsky et al.[12] arrived at a similar failure surface, albeit with two distinct restrictions. Although their analysis included a different set of geometric parameters, the two restrictions, in terms of parameters used in this paper, were: $r_0'/r_0 = 0$, i.e., the upper log-spiral in Fig. 1 is reduced to a point, and $r_c \leq r_s$, i.e., the center line of the curvilinear cone cannot intersect the slope. Leshchinsky et al.[12] reported their 3D results in a graph as a stability number (Eq. (18)); their solution is compared in Fig. 3 to the 3D asymptotic solution calculated based on the alternative mechanism shown in Fig. 2, and to the 2D solution. Not surprisingly, the 2D solution yields the more critical outcome than either of the 3D solutions (the higher the stability

number the more accurate the result as the kinematic approach yields the lower bound to the stability number in Eq. (18)).

3.2. *A mechanism with an insert*

In order to allow the 3D solution to approach the 2D solution in the absence of restrictions on the size of the mechanism, an insert with 2D geometry is included, as shown in Fig. 4. Such a modification was used earlier by Baligh and Azzouz[5] and Leshchinsky and Baker[45] in the limit equilibrium analysis, and also by Michalowski and Drescher[14] in the limit analysis approach. The reader will notice the "overhanging" region in the stationary material when the center line of the curvilinear cone intersects the slope ($r_c > r_s$). The work dissipation and the work rate of the soil weight in the insert were calculated using a well-known procedure[31], and the respective expressions are not reproduced here. Figure 5 illustrates the trace of three possible variations of the collapse mechanism: toe failure, below-toe failure, and the face collapse. Depending on the limitation on the width of the mechanism, the most critical toe and below-toe mechanisms may include the insert, but the face failure mechanisms never do. This is illustrated in an example solution in Fig. 6 for a 60-degree slope and $\phi = 30°$. Without any limitation on the mechanism width, the failure pattern tends to a 2D mechanism reaching the toe (or below the toe for small slope inclinations). In this particular case, the stability number (Eq. (18)) from the 2D solution is 0.062. Once the limitation on the width is imposed, the plane insert in the most critical mechanism is progressively reduced with a drop in the mechanism width (drop in ratio B/H; B – width, H – slope height), until the 2D insert is reduced to zero (at about $B/H = 0.78$). With further decrease in the width of the mechanism, the critical toe mechanism (without insert) slightly changes its shape due to width reduction, until such ratio $(B/H)^*$ where an admissible toe mechanism can no longer be constructed. In this particular example, this occurs at $B/H = 0.65$, beyond which only a face mechanism can fit into the narrow space. This is why the critical face mechanisms do not include plane inserts. The dimensionless width at that transition is defined as

$(B/H)^*$, with associated stability number N_n^*. For this specific example: N_n^* = 0.032. The stability number for narrower slopes can be simply determined from

$$\frac{c}{\gamma H} = N_n^* \frac{\frac{B}{H}}{\left(\frac{B}{H}\right)^*} = N_n^* \left(\frac{H}{B}\right)^* \frac{B}{H} \tag{20}$$

where B/H is the limitation on the slope width ($B/H < (B/H)^*$). Because the starred quantities are constant for a given slope, Eq. (20) is linear in B/H, as illustrated by the dashed line in Fig. 6. The dots on the dashed line represent independent computations for varying heights h ($h < H$) of the mechanism (see Fig. 5 for h).

4. CALCULATED RESULTS

An upper bound to the stability factor in Eq. (17) was calculated using the work rate balance in Eq. (10) with the two terms described in Eqs. (16) and (13). Additionally, the respective terms for the plane insert[31] were added to account for wide mechanisms. The variable parameters in the process of minimizing the stability factor were angles θ_0, θ_h, θ_C (the latter for below-toe failure only), and ratio r_0 / r_0' (see Fig. 1). Angles θ_i were varied with a minimum increment of 0.01° and ratio r_0 / r_0' was varied with a minimum of 0.001. The iteration was stopped when the difference between the two consecutive solutions was less than 10^{-6}. The first set of results is presented in Fig. 7. Stability numbers (reciprocal of stability factors) are shown as functions of $\tan\phi$ for slope angles varying from 30° to 90°, and for different limitations B/H on the width of the mechanism. Such presentation is convenient, because it allows for easy reading of the factor of safety F defined as

$$F = \frac{c}{c_d} = \frac{\tan\phi}{\tan\phi_d} \tag{21}$$

where subscript *d* stands for *developed* (mobilized) strength parameters at failure. This procedure is described briefly in the Appendix.

In the case of undrained failure, the failure surface reduces to a torus. Numerical values of the stability factors for undrained failure $\gamma H/s_u$ are compared in Table 1 to those in Gao et al.[17] and Zhang et al.[19] (Zhang et al. presented numerical values of stability numbers, so they were converted into stability factors). The results given in [17] follow the analysis presented originally in Michalowski and Drescher[14], though Gao et al.[17] used a more efficient minimization procedure. The largest difference in the results produced in this paper and those in [17] and [19] is for narrow slopes. For instance, for $B/H = 0.5$ and undrained failure, Gao et al.[17] overestimate the result in this study by about 33% for a gentle slope of 30°, and by about 27% for a vertical slope. The largest overestimation of almost 39% was found for a 30-degree slope and $B/H = 0.6$. However, this overestimation drops to no more than 2% when $B/H = 3$. Zhang et al. (2016) did not report the results for $B/H < 1.5$. Because the kinematic analysis yields an upper bound to the stability factor, the lower estimates in Table 1 are more accurate. The most likely reason for overestimating the results in Gao et al.[17] and Zhang et al.[19] is excluding mechanisms that would allow the center line of the torus to intersect the slope. This limitation on the geometry of the mechanism was imposed in both papers[17,19], even though a different method of solution was used. This limitation was also used in the paper of Michalowski and Drescher[14], but this restriction is relaxed in this study. A graphical illustration of this limitation is presented in Fig. 8 using an example of undrained failure of a 30° slope limited to width ratios $B/H = 0.5$ and $B/H = 0.8$. The said limitation can be mathematically described as

$$r_s \geq r_c \tag{22}$$

where r_s is the radius tracing the contour of the slope given in Eq. (6), and r_c is the radius of the central line of the torus given in Eq. (5). The central line of the torus is traced with a dashed line

in Fig. 8. The geometry of the failure mechanism for $H/B = 0.5$ is illustrated in Figs. 8(a) and (b) with the restriction in Eq. (22) and without, respectively. The most critical mechanism was found when the restriction in Eq. (22) is not enforced; it is a toe mechanism illustrated in Fig. 8(b), which has the lowest stability factor $\gamma H/s_u = 16.65$. When the constraint in Eq. (22) is enforced, the best failure mechanism appears to be a face failure as in Fig. 8(a), with $\gamma H/s_u = 20.79$. Gao et al.'s solution in [17] used the limitation in Eq. (22), and they found the face failure to be critical, but their solution appears to be less accurate ($\gamma H/s_u = 22.10$, Fig. 8(a)), and it overestimates the best solution in this paper (Fig. 8(b)) by almost 33%. Zhan et al.[19] did not produce results for B/H less than 1.5; they only considered mechanisms with an additional limitation $r' = 0$, and only toe failures. Calculations revealed that with these two limitations, one cannot fit an admissible toe mechanism in a narrow slope such as that with a width ratio $B/H = 0.5$.

It is interesting to investigate an undrained failure of a slightly wider 30° slope, $B/H = 0.8$. The most critical mechanism found now is an under-toe failure, $\gamma H/s_u = 12.17$, whereas the solution offered by Gao et al.[17] is a face failure with $\gamma H/s_u = 15.38$, a 26% overestimation. If the limitation in Eq. (22) is used in the solution offered in this paper, the critical mechanism is a toe failure, and with $\gamma H/s_u = 14.60$ still more accurate than the solution in [17], Fig. 8(c). The specific geometric parameters defining the solutions in Fig. 8 are given in Table 2. The precision of three digits after the decimal point in all tables is given only for comparative reasons.

Comparisons of stability factors for $\phi = 15°$ and $\phi = 30°$ are presented in Tables 3 and 4. In all cases the current study provides lower stability factors, but the differences are less than 6% and in many cases less than 1%.

In all results presented in the tables, the least upper bound to the stability factor was reported. Whether this critical solution is a toe failure, below-toe, or a face failure depends on the

combination of the slope inclination angle (β), internal friction angle (ϕ), and the slope width limitation (B/H). The three collapse patterns are marked in the graph in Fig. 9.

4.1. *An influence of seepage*

Previous results were presented for slopes with no seepage. In the absence of known specific hydraulic conditions, coefficient r_u (Bishop and Morgrnstern[46]) is used as a generic means to compare the influence of the presence of pore water pressure for different slopes. This coefficient yields the distribution of the pore water pressure, and the work of this pore water pressure on the volumetric strain of the soil during plastic deformation can be proved to be equal to the work of the buoyancy and the seepage forces[47,48]. Because the plastic deformation occurs only along the failure surface in the mechanism considered, the rate of work of the pore water pressure W_u on the volumetric strain of the soil can be calculated as

$$W_{\mathrm{u}} = \int_L uv\sin\phi dL \tag{23}$$

where u is the pore water pressure determined from given coefficient r_u, v is the magnitude of velocity jump vector on the failure surface, ϕ is the internal friction, and L is the area of the failure surface. The expression in Eq. (23) was included on the right-hand side of the balance in Eq. (10), and the results of calculations are shown in Fig. 10.

4.2. *An influence of quasi-static seismic force*

Although considering the seismic effects requires dynamics computations, a rough estimate of the vulnerability of slopes to seismic shaking can be considered using a quasi-static approach where the dynamic effects are substituted with a static horizontal load. The intensity of this load is defined by the coefficient of horizontal acceleration k_h. The seismic influence is then included as additional work done by inertial forces. This rate of work, W_S, can be calculated analogously to the rate of soil weight in Eq. (11)

$$W_S = k_h \int_V \gamma v \sin\theta dV \tag{24}$$

This term was included on the right side of the work rate balance in Eq. (10), and the results of computations are illustrated in Fig. 11.

5. DISCUSSION

Kinematic limit analysis is an effective method to assess safety of slopes. Its limitations come from difficulties in considering non-homogeneities in material properties and complex geometries of slopes. Numerical approaches are more efficient in these cases, e.g., Li et al.[25], but for simple slopes, the approach presented in this paper typically yields better results[15,19].

The focus of the discussion is on the sources of discrepancies in the solution results presented in the literature, solutions that come apparently from considering the same failure mechanism. The results based on the procedure presented in this paper were compared to those of Gao et al.[17] in Section 4. Their results were based on the same algorithm as that in [14]. The largest discrepancies, up to 39%, were found for narrow slopes failing in an undrained manner. The differences, however, became less significant with an increase in the width of the mechanism of failure and with an increase in the internal friction angle. More comprehensive comparison is

presented graphically in Fig. 12. The results were presented in [17] in terms of the stability factor, and they were converted to the stability number in order to have all graphs presented in a consistent manner (the bullets are the converted numerical values of stability factors and the dashed lines are converted from the graphs in [17]).

Zhang et al.[19] have not presented results for narrow slopes, where the discrepancies between the results produced in this paper and those in [17] were found to be the largest. Their considerations were subject to three constraints: $r' = 0$, $r_s \geq r_c$ (see Fig. 1 for r', r_s, and r_c), and toe failures only. With these constraints, one cannot fit admissible rotational mechanisms in narrow slopes, e.g., $H/B = 0.5$. The comparison in Fig. 13 is then presented for $B/H = 1.5$, the smallest width for which the results were reported in [19].

When slopes are not subjected to seismic loads, a substantial difference occurs only for very steep slopes failing in an undrained manner. If substantial seepage is accounted for ($r_u = 0.5$), the considerable difference occurs for very steep slopes and large internal friction angles. When slopes are subjected to seismic loads, the results for steep slopes failing in undrained process show the largest discrepancy. In all cases the analysis presented in this paper provides more accurate results (the kinematic approach yields the lower bound to the stability number, thus the larger the stability number the more accurate the solution).

To reveal the causes of discrepancies among different solutions we consider the influence of assumptions used in different analyses on the geometry of the critical mechanisms and on the outcome in terms of the stability factor. Consider an undrained failure of a vertical slope with width defined by $B/H = 1.5$. The two graphs (upper and lower) in Fig. 14(a) present a cross section of the critical mechanism from the analysis where the inner diameter of the torus was set to zero, $r' = 0$, and the center line of the torus was not to intersect the slope, $r_s \geq r_c$. With these limitations the algorithm proposed in this paper converged to a minimum of $\gamma H/s_u = 5.41$, which

is equivalent to a stability number (reciprocal of stability factor) equal to 0.185. This is exactly the result reported in [19], where the authors used the two restrictions. The center line of the torus forming the failure surface is tangent to the slope crest, which is enforced by limitation $r_s \geq r_c$. The solution illustrated in Fig. 14(b) was obtained when limitation $r' = 0$ was relaxed, but the restraint $r_s \geq r_c$ was still enforced. The solution is now improved, with $\gamma H/s_u$ = 5.38, the same stability factor as reported in [17] where the same limitations were used. If limitation $r_s \geq r_c$ is relaxed but the inner radius of the torus is set to zero, $r' = 0$, the solution becomes $\gamma H/s_u$ = 5.37 (Fig. 14(c)), but the best solution is obtained when both restrictions on the geometry are removed, as in Fig. 14(d), where $\gamma H/s_u$ = 5.19. In this particular case, the numbers reported in [17] and [19] overestimate the result calculated in this study by only a little more than 4%, but the difference becomes much larger for narrower slopes, as shown in Table 1.

6. CONCLUSIONS

The geometry of the mechanism postulated in the kinematic approach of limit analysis for assessing the safety of slopes plays a crucial role. While construction of mechanisms with two-dimensional geometry is relatively straightforward, three-dimensional (3D) mechanisms can be intricate due to their complicated geometry. 3D rotational mechanisms with a failure surface in a shape of a curved cone, or a torus for undrained failures, have been used in past studies. It was demonstrated in this paper that two assumptions used in previous studies of 3D slope failures lead to limitations that exclude the most critical failure mechanisms for some range of slope parameters.

An early example of a rotational 3D collapse pattern was described by Leshchinsky et al.[12], and it was derived by a variational approach used as a means of finding the most critical mechanism. A more general class of admissible failure surfaces can be defined as curvilinear cones, or "horn-shape" surfaces. They can be generated by rotating a circle of increasing diameter about an axis[14]. The surface found in [12] is a special case of such a surface when the axis about which

the generating circle revolves is tangent to the circle, Fig. 15(a), which is a limitation on the multiplicity of admissible surfaces. The second limitation found in earlier analyses[14,17] was in the requirement that the center line of the generated surface would not intersect the slope. These limitations affected the assessment of slope safety, and also did not allow finding admissible 3D collapse mechanisms for narrow slopes. The mechanism in the paper by Michalowski and Drescher[14] was independently postulated based on admissibility of the kinematic field; this mechanism was later adopted by others.[17] Although the mechanisms in [12] and [14] are based on different premises, their geometry is essentially the same, with the exception of the limitations already mentioned. Zhang et al.[19], who more recently presented both approaches, pointed out that an improvement of the results due to removing the first limitation is negligible for wider slopes ($B/H \geq 1.5$). In the study presented in this paper both limitations were removed, Fig. 15(d), and it was found that these restrictions have very significant consequences for narrow slopes. The largest difference was found for an undrained failure of a narrow slope with $B/H = 0.6$; the stability factor found by Gao et al.[17] overestimates the one in this study by almost 39% (Table 1). Such a large difference was found because removing both limitations widens the range of slope parameters for which admissible failure mechanisms can be found. In general, substantial differences exist for undrained failures in narrow slopes ($B/H \leq 1.0$). The study by Zhang et al.[19] did not produce solutions for narrow slopes, because only toe failures were sought, and with the limitations imposed on the geometry of the slope collapse, admissible rotational mechanisms could not be found. The comparisons of results produced in this study and those from previous studies allow concluding that the discrepancies among published results for 3D slope stability analyses come from limitations imposed on the collapse mechanisms used in some of the approaches.

The solution discussed in this paper falls under the category of semi-analytical as the numerical calculations were only used in the optimization phase of the analysis. The numerical approach using finite elements in limit analysis[49,50] is a method that has some advantages over the semi-

analytical approach; for example, geometric complexities and material non-homogeneities are easier to account for. However, the solutions to homogeneous slopes with simple geometry appear to be more accurate when using the semi-analytical approach, as demonstrated in [19]. This appears to be true also for other limit-state geotechnical problems[27].

7. NOTATION

D	-	rate of internal work (dissipated work)
H	-	slope height
L	-	area of velocity discontinuity surface
N_f	-	stability factor $\gamma H/c$
N_n	-	stability number $c/\gamma H$
R	-	radius of the nonlinear cone cross section
S	-	area of a surface
T_i	-	stress vector
V	-	volume of the mechanism
W_s	-	rate of work of inertial (seismic) forces
W_u	-	rate of work of pore water pressure on volumetric strain of soil
W_γ	-	rate of work of soil weight
X_i	-	distributed load vector
c	-	cohesion of bonded soil
k_h	-	coefficient of horizontal acceleration
r	-	radius of the failure surface at the central cross section
r'	-	upper radius of the conical surface
r_c	-	radius of the curvilinear cone centerline
r_s	-	radius defining the contour of the slope
r_u	-	pore water pressure coefficient
s_u	-	undrained shear strength
$[v]_i$	-	velocity jump vector on a failure surface
v_i	-	velocity vector
v	-	magnitude of the velocity vector
γ	-	unit weight
$\dot{\varepsilon}_{ij}^{pl}$	-	plastic strain rate tensor

θ - angular coordinate

ρ - radial coordinate

σ_{ij} - stress tensor

ϕ - internal friction angle

ω - angular velocity

Acknowledgement

The work presented in this paper was carried out when the authors were supported by the National Science Foundation through grant No. 1537222 from the Division of Civil, Mechanical and Manufacturing Innovation. This support is gratefully acknowledged.

APPENDIX

The stability factor or stability number in Eqs. (17) or (18) are often used as the means of assessment of the slope safety, but more often the factor of safety in Eq. (21) is required in geotechnical design. Extracting the factor of safety from the stability factor (or stability number) typically requires an iterative procedure (except in cases of undrained collapse). A convenient manner of presenting the results without the need for iterations was shown earlier[51]. An alternative way is illustrated here, where the stability number is reported as a function of $\tan\phi$, as in Figs. 7, 10, and 11. Inferring the factor of safety from the graphs is explained in an example illustrated in Fig. 7(b).

Consider a 10-m tall (H) slope, 15 m in width (B), with inclination angle of 60° (β), and the following material properties: γ = 17 kN/m^3, c = 20 kN/m^2, and ϕ = 15°. Hence $\tan\phi$ = 0.268 and the noncritical dimensionless group $c/\gamma H$ for this (safe) slope is 0.118. Now, mark a point on the

graph with coordinates 0.268 and 0.118 (upper open circle), and draw a straight line through it and the origin of the chart. Find the intersection point of this line with the curve for $\beta = 60°$ and $B/H = 1.5$ (lower open circle). The ratio of the length from the origin to the upper circle to the length connecting the origin and the lower circle is the factor of safety; in this case $F \approx 1.20$.

REFERENCES

1. Collin, A. Recherches Expérimentales sur les Glissements Spontantés des Terrains argileux. Paris: Carilian-Goeury; 1846. 160 p. Translation by W.R. Schriever: Landslides in Clays. University of Toronto Press, 1956.
2. Fellenius, W. Erdstatische Berechnungen mit Reibungund und Kohäsion (Adhäsion) und unter Annahme kreiszylindrischer Gleitflächen. Berlin: Ernst & Sohn; 1927. 40 p. Translation from the Swedish edition, Stockholm 1926.
3. Taylor, D.W. Stability of earth slopes. J. Boston Society of Civil Engineers 1937; 24, No. 3. Reprinted in: Contributions to Soil Mechanics 1925 to 1940. Boston Society of Civil Engineers, 337-386.
4. Drucker, D.C., Prager, W. Soil mechanics and plastic analysis or limit design. Quart Appl Math 1952; 10: 157-165.
5. Baligh, M.M., Azzouz, A.S.. End effects on stability of cohesive slopes. ASCE J Geot Eng Div 1975; 101: 1105-1117.
6. Gens, A., Hutchinson, J.N., Cavounidis, S. Three-dimensional analysis of slides in cohesive soils. Géotechnique 1988; 38: 1-23.
7. Hovland, H. J. Three dimensional slope stability analysis method. J Geotech Eng Div 1977; 103: 971-986.
8. Hungr, O. An extension of Bishop's simplified method of slope stability analysis to three dimensions. Géotechnique 1987; 37: 113-117.
9. Lam, L., Fredlund, D.G. A general limit equilibrium model for three-dimensional slope stability analysis. Can Geotech J 1993; 30: 905-919.
10. Drescher, A. Limit plasticity approach to piping in bins. J Appl Mech 1983; 50: 549-553.
11. Michalowski, R.L. Three-dimensional analysis of locally loaded slopes. Géotechnique 1989; 39: 27–38. doi:10.1680/geot.1989.39.1.27.
12. Leshchinsky, D., Baker, R., Silver, M.L. Three dimensional analysis of slope stability. Int J Num Analyt Meth Geomech 1985; 9:199–223.

13. De Buhan, P., Garnier, D. Three dimensional bearing capacity analysis of a foundation near a slope. Soils and Foundations 1998; 38: 153-163.
14. Michalowski R.L., Drescher A. Three-dimensional stability of slopes and excavations. Géotechnique 2009; 59: 839–850.
15. Michalowski, R.L. Limit analysis and stability charts for 3D slope failures. J Geotech Geoenv Eng 2010; 136: 583-593.
16. Michalowski, R.L. and Martel, T. Stability charts for 3D failures of steep slopes subjected to seismic excitation. J Geotech Geoenv Eng 2011; 137: 183-189.
17. Gao, Y. F., Zhang, F., Lei, G. H., and Li, D. Y. An extended limit analysis of three-dimensional slope stability. Géotechnique 2013; 63: 518-524.
18. Nadukuru, S.S. and Michalowski, R.L. Three-dimensional displacement analysis of slopes subjected to seismic loads. Can Geotech J 2013; 50: 650-661.
19. Zhang, F., Leshchinsky, D., Baker, R., Gao, Y., Leshchinsky, B. Implications of variationally derived 3D failure mechanism. International Journal for Numerical and Analytical Methods in Geomechanics 2016; 40: 2514-2531.
20. Bekaert, A. Improvement of the kinematic bound for the stability of a vertical cut-off. Mech Res Com 1995; 22: 533-540.
21. Griffiths, D.V., Marquez, R.M. Three-dimensional slope stability analysis by elasto-plastic finite elements. Géotechnique 2007; 57: 537-546.
22. Borja, R.I., Liu, X., White, J.A. Multiphysics hillslope processes triggering landslides. Acta Geotechnica 2012; 7: 261-269.
23. Camargo, J., Velloso, R.Q., Vargas, E.A. Numerical limit analysis of three-dimensional slope stability problems in catchment areas. Acta Geotechnica 2016; 11: 1369-1383.
24. Hicks, M.A., Li, Y. Influence of length effect on embankment slope reliability in 3D. Int J Numer Anal Methods Geomech. 2018; 42: 891–915.
25. Li, A.J., Merifield, R.S., Lyamin, A.V. Three-dimensional stability charts for slopes based on limit analysis methods. Can Geotech J 2010; 47: 1316–1334.

26. Lim, K., Li, A.J., Lyamin, A.V. Three-dimensional slope stability assessment of two-layered undrained clay. Computers and Geotechnics 2015; 70: 1-17.
27. Michalowski, R.L. Collapse loads over two-layer clay foundations soils. Soils and Foundations 2002; 42: 1-7.
28. Tun, Y.W., Llano-Serna, M.A., Pedroso, D.M., Scheuermann, A. Multimodal reliability analysis of 3D slopes with a genetic algorithm. Acta Geotechnica 2018; https://doi.org/10.1007/s11440-018-0642-9
29. Hill, R. Mathematical Theory of Plasticity. Oxford: Clarendon Press; 1950. 355 p.
30. Salençon, J. Applications of the theory of plasticity in soil mechanics. (Translated from 1974 French edition.) New York, Wiley; 1977. 158 p.
31. Chen, W.F. Limit analysis and soil plasticity. Amsterdam: Elsevier; 1975. 638 p.
32. Mróz, Z. Non-associated laws in plasticity. J Mécanique 1963; 2: 21-42.
33. Radenkovic, D. Théorie des charges limites extension a la mécanique des sols. Séminaire de Plasticité. École Polytechnique, Publications Scientifiques et Techniques du Ministère de L'Air 1961; published 1962: 129-141.
34. Palmer, A.C. A limit theorem for materials with nonassociated flow law. J Mécanique 1966; 5: 217-222.
35. Collins, I.F. The upper bound theorem for rigid/plastic solids generalized to include Coulomb friction. J. Mech. Phys. Solids 1969; 7: 323-338.
36. Mróz, Z., Drescher, A. Limit Plasticity Approach to Some Cases of Flow of Bulk Solids. ASME J Eng Ind 1969; 91: 357-364
37. Michalowski, R.L and Mróz, Z. Associated and non-associated sliding rules in contact friction problems. Arch Mech Stos (Archives of Mechanics) 1978; 30: 259-276.
38. Drescher, A. Detournay, E. Limit load in translational failure mechanisms for associative and non-associative materials. Géotechnique 1993; 43: 443-456.
39. Salençon, J. An introduction to the yield design theory and its applications to soil mechanics. Eur. J. Mech., A/Solids 1990; 9: 477-500

40. Hoek, E., Bray, J.W. Rock Slope Engineering. 2nd Edition. London: Institution of Mining and Metallurgy; 1981. 360 p.
41. Michalowski, R.L. Upper-bound load estimates on square and rectangular footings. Géotechnique 2001; 9: 787-798.
42. Yang, X., Li, Z. Kinematical analysis of 3D passive earth pressure with nonlinear yield criterion. Int J Numer Anal Methods Geomech. 2018; 42: 916–930.
43. Park, D., Michalowski, R.L. Three-dimensional stability analysis of slopes in hard soil/soft rock with tensile strength cut-off. Engineering Geology 2017; 229: 73-84
44. Park, D., Michalowski, R.L. A cone surface in 3D analyses of slopes with tension cut-off. Geotechnical Research 2018; 5: 51-67.
45. Leshchinsky, D, Baker R. Three-dimensional slope stability: end effects. Soils Found 1986; 26: 98–110.
46. Bishop AW, Morgenstern N. Stability coefficients for earth slopes. Géotechnique 1960; 10: 129–150.
47. Michalowski, R.L. (1995). Slope stability analysis: a kinematical approach. Géotechnique 45 No. 2, 283-293.
48. Viratjandr, C., Michalowski, R.L. Limit analysis of slope instability caused by partial submergence and rapid drawdown. Canad Geotech J 2006; 43: 802-814.
49. Pastor, J. Analyse limite: determination numerique de solutions statiques completes. Application au talus vertical. J Mech Appl 1978; 2: 167-196.
50. Sloan, S.W. Upper bound limit analysis using finite elements and linear programming. Int J Num Analyt Meth Geomech 1989; 13: 263–282.
51. Michalowski, R.L. Stability charts for uniform slopes. J Geotech Geoenv Eng 2002; 128: 351-355.

Figure Captions

Figure 1. Three-dimensional rotational failure mechanism generated by revolving a circle of increasing diameter about an axis passing through point O.

Figure 2. Alternative mechanism generated by revolution of a circle with increasing diameter about a chord.

Figure 3. Comparison of 3D solutions from [12] to the 3D asymptotic solution in this study based on the alternative mechanism in Fig. 2.

Figure 4. Rotational mechanism with an insert with 2D geometry.

Figure 5. Trace of three types of possible failure patterns.

Figure 6. Dependence of the failure type on the relative slope width.

Figure 7. Stability number for slopes as function of $\tan\phi$ for slopes with inclination 30° to 90°: (a) for narrow slopes, $B/L \leq 1.0$, and (b) for wide slopes, $B/L \geq 1.5$.

Figure 8. Discussion of critical collapse patterns for undrained failure in narrow slopes (slope inclination 30°).

Figure 9. Dependence of the failure pattern on the slope inclination and the soil internal friction angle.

Figure 10. Stability number for slopes in the presence of seepage for slopes with inclination 30° to 90°: (a) $r_u = 0.25$ and narrow slopes, $B/L \leq 1.0$, (b) $r_u = 0.25$ and slopes, $B/L \geq 1.5$, (c) $r_u = 0.5$ and narrow slopes, $B/L \leq 1.0$, and (d) $r_u = 0.5$ and wide slopes, $B/L \geq 1.5$

Figure 11. Stability number for slopes subjected to horizontal acceleration: (a) $k_h = 0.1$ and narrow slopes, $B/L \leq 1.0$, (b) $k_h = 0.1$ and wide slopes, $B/L \geq 1.5$, (c) $k_h = 0.2$ and narrow slopes, $B/L \leq 1.0$, (d) $k_h = 0.2$ and wide slopes, $B/L \geq 1.5$, (e) $k_h = 0.3$ and narrow slopes, $B/L \leq 1.0$, and (f) $k_h = 0.3$ and wide slopes, $B/L \geq 1.5$.

Figure 12. Comparison of calculated stability numbers to those in [17] for slopes of different widths.

Figure 13. Comparison of calculated stability numbers to those in [19] for selected seepage and seismic acceleration, for $B/H = 1.5$.

Figure 14. Explanation of the impact of geometrical limitations on the outcome of the analysis.

Figure 15. (a) The shape of a failure surface with limitation $r' = 0$, and (b) failure surface allowing $r' > 0$, and also permitting the center line (dashed) to intersect the slope.

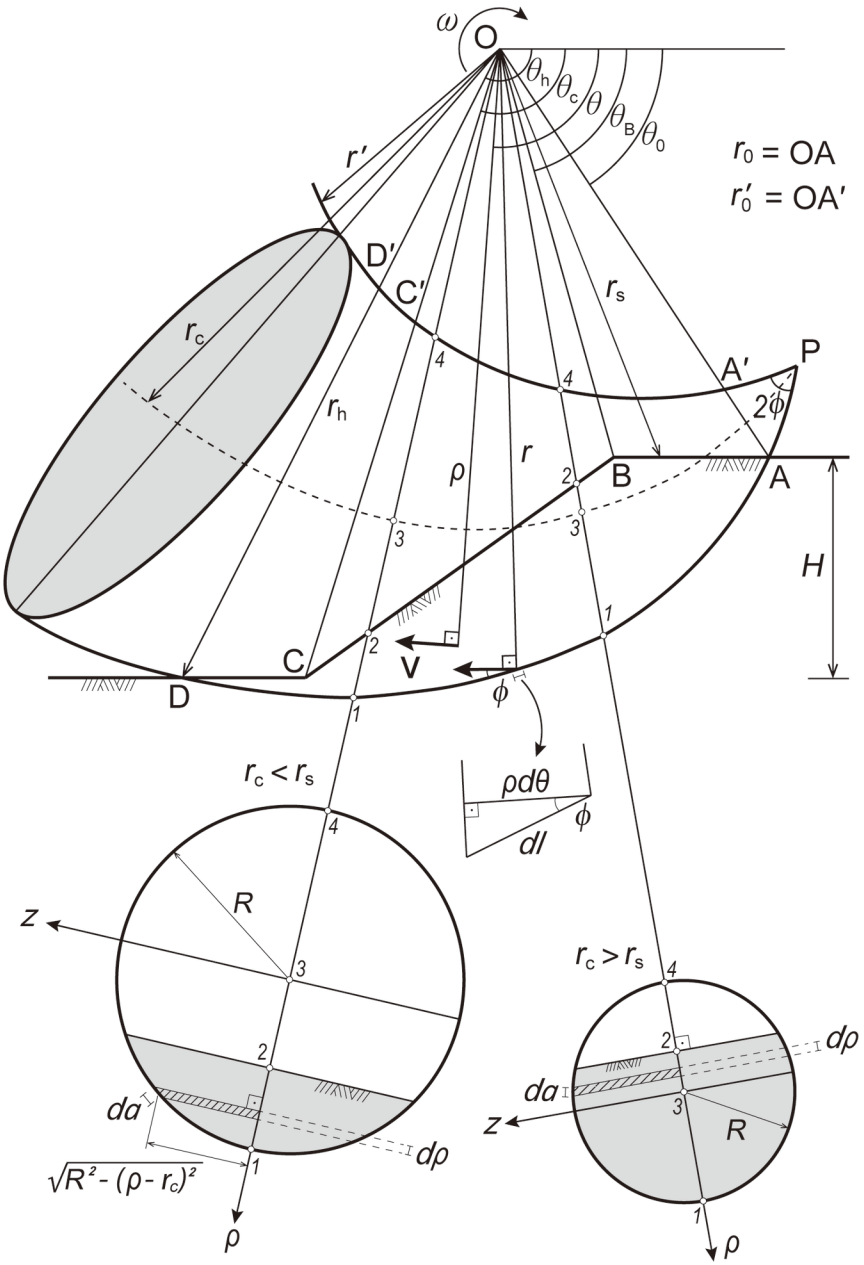

NAG_2846_Figure 1.tif

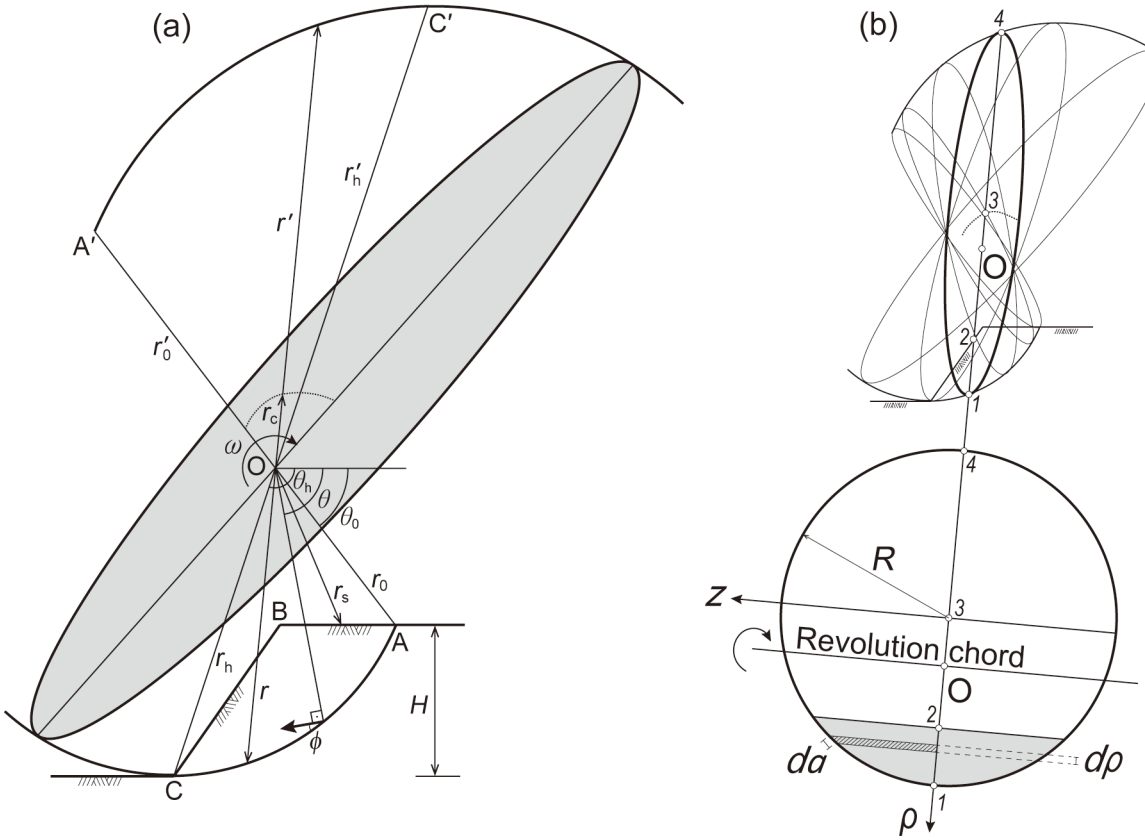

NAG_2846_Figure 2.tif

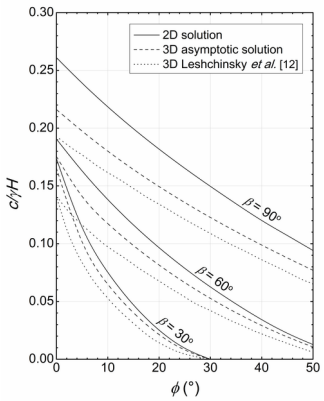

NAG_2846_Figure 3.tif

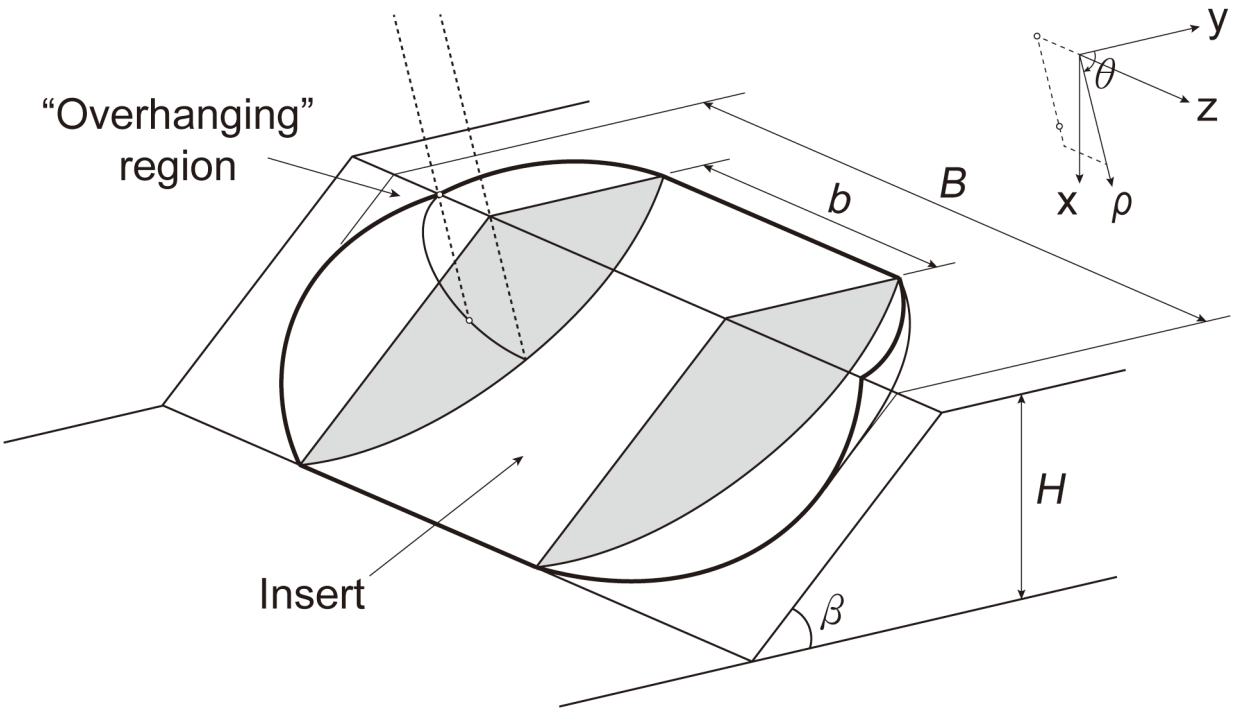

NAG_2846_Figure 4.tif

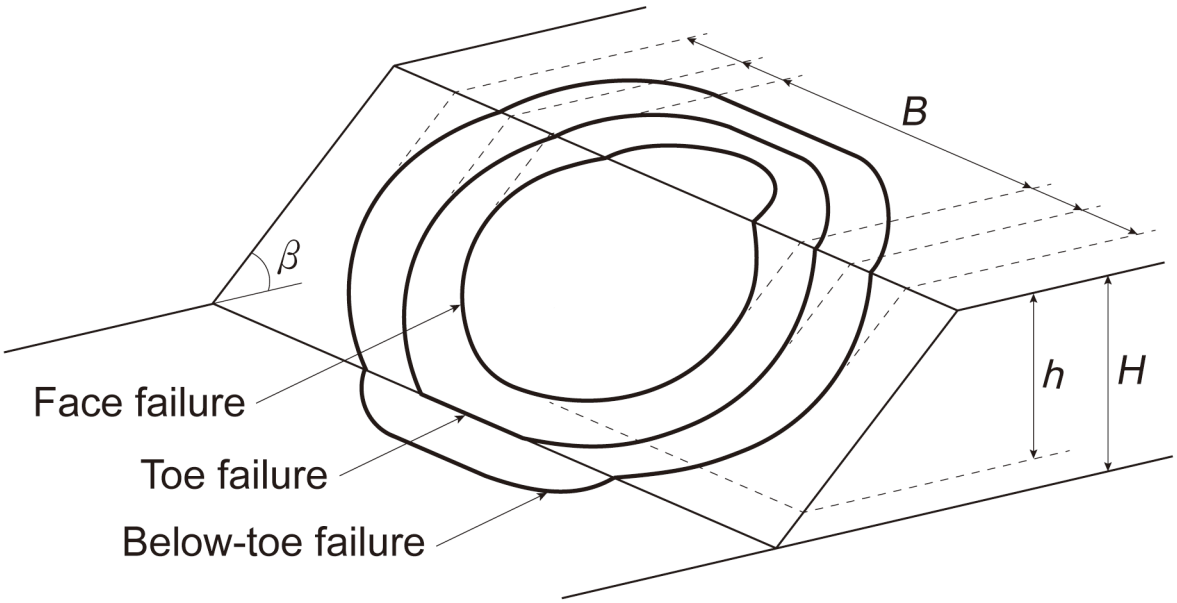

NAG_2846_Figure 5.tif

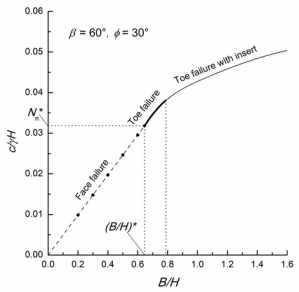

NAG_2846_Figure 6.tif

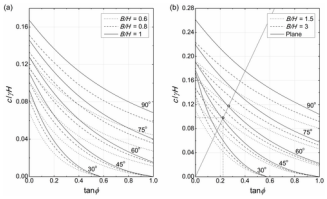

NAG_2846_Figure 7.tif

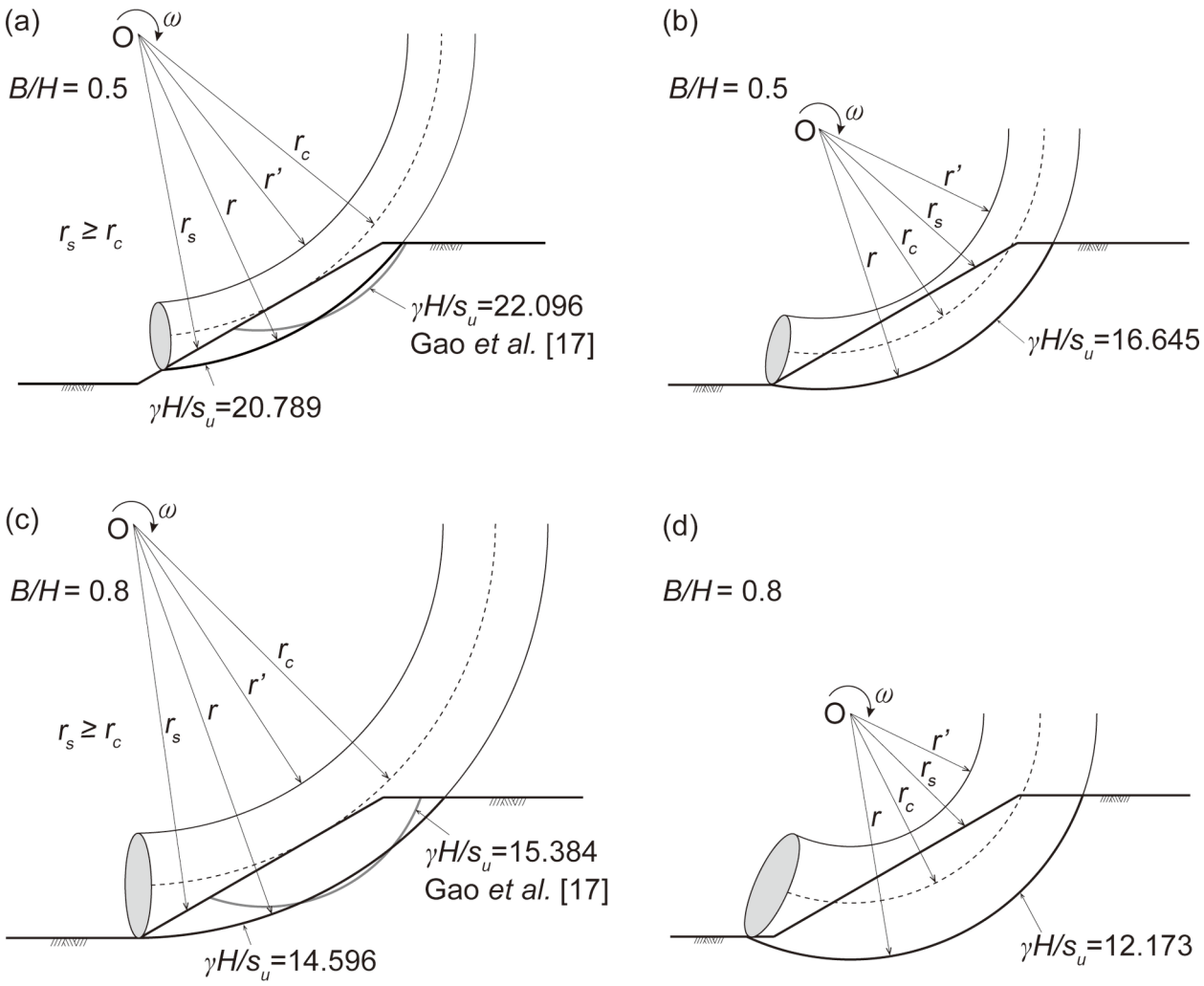

NAG_2846_Figure 8.tif

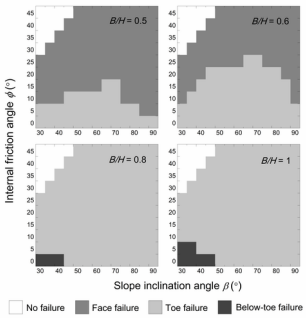

NAG_2846_Figure 9.tif

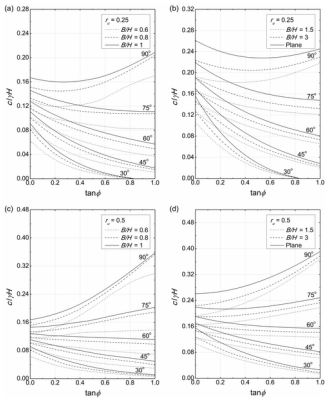

NAG_2846_Figure 10.tif

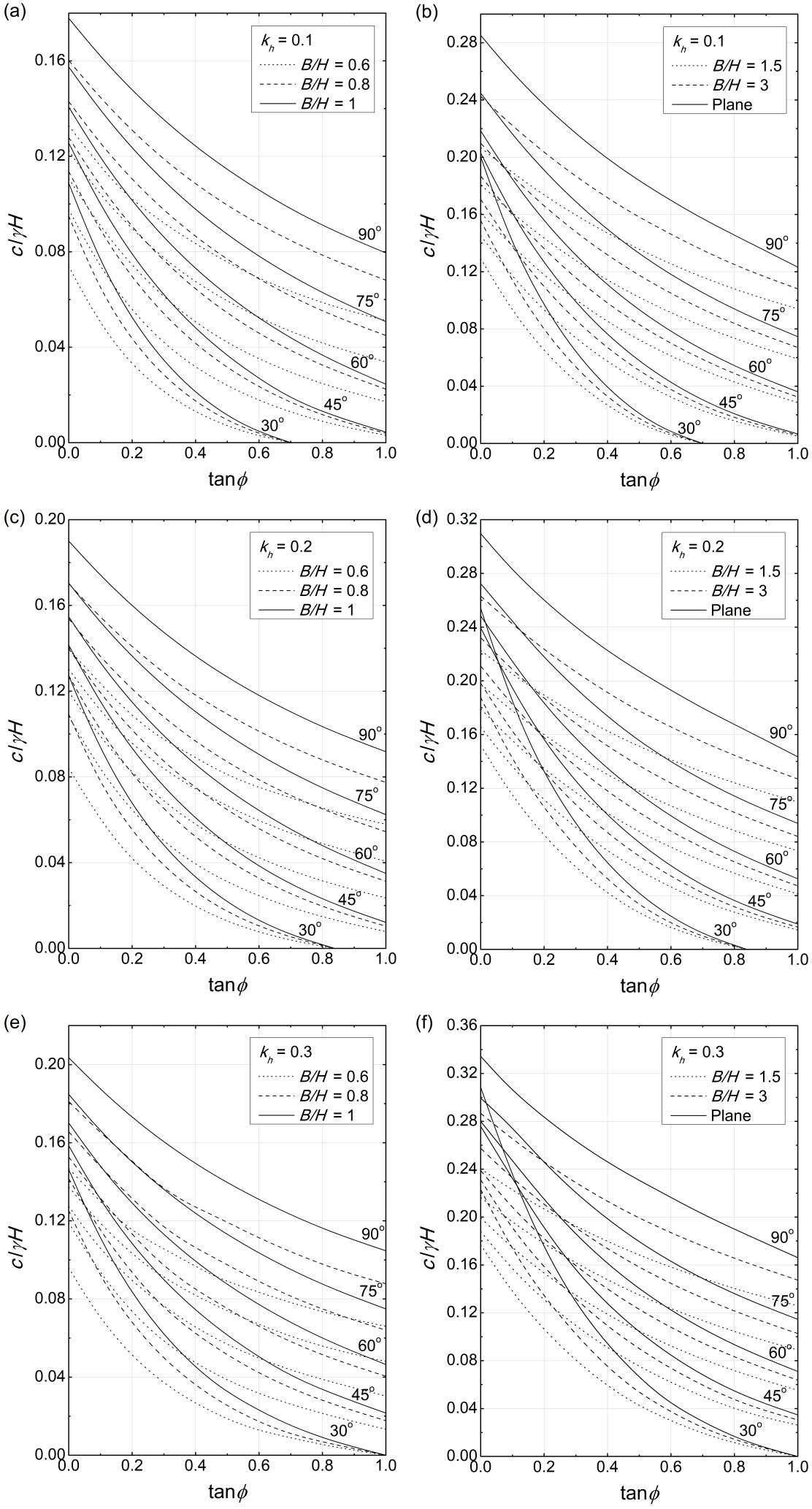

NAG_2846_Figure 11.tif

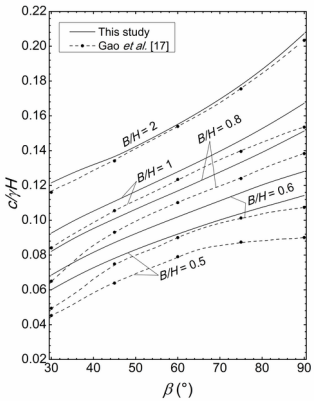

NAG_2846_Figure 12.tif

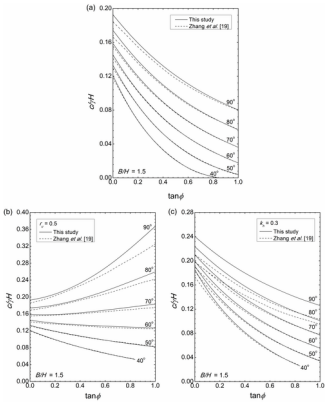

NAG_2846_Figure 13.tif

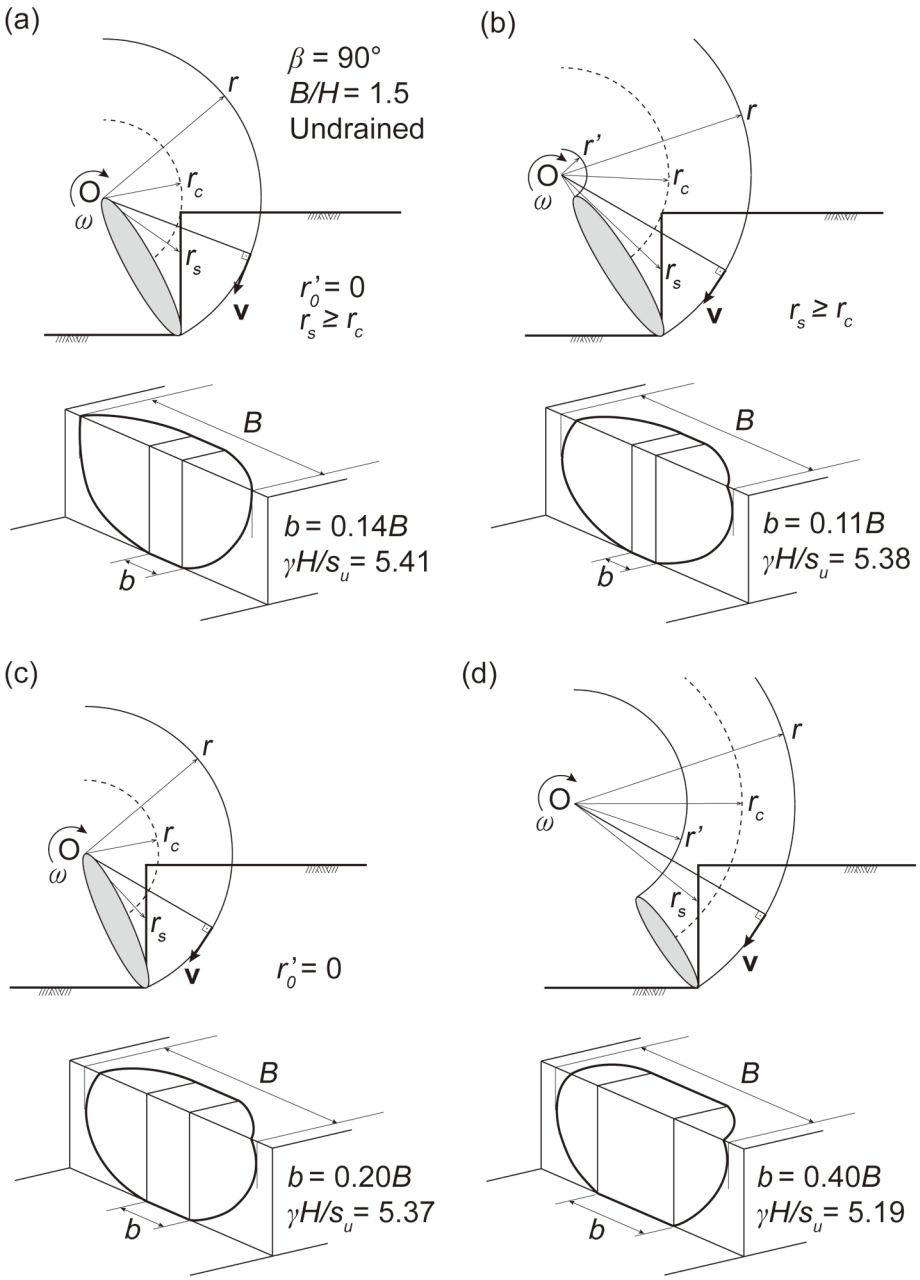

NAG_2846_Figure 14.tif

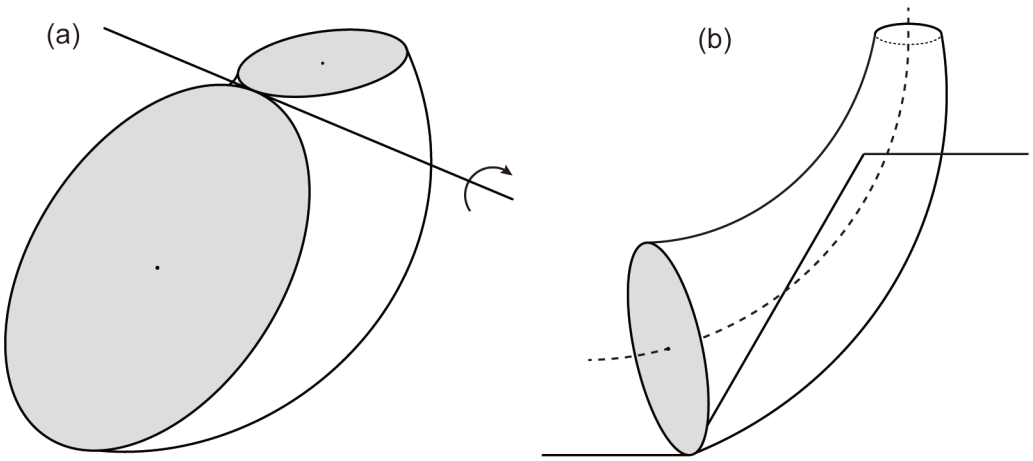

NAG_2846_Figure 15.tif

Figure Captions

Figure 1. Three-dimensional rotational failure mechanism generated by revolving a circle of increasing diameter about an axis passing through point O.

Figure 2. Alternative mechanism generated by revolution of a circle with increasing diameter about a chord.

Figure 3. Comparison of 3D solutions from [12] to the 3D asymptotic solution in this study based on the alternative mechanism in Fig. 2.

Figure 4. Rotational mechanism with an insert with 2D geometry.

Figure 5. Trace of three types of possible failure patterns.

Figure 6. Dependence of the failure type on the relative slope width.

Figure 7. Stability number for slopes as function of $\tan\phi$ for slopes with inclination 30° to 90°: (a) for narrow slopes, $B/L \leq 1.0$, and (b) for wide slopes, $B/L \geq 1.5$.

Figure 8. Discussion of critical collapse patterns for undrained failure in narrow slopes (slope inclination 30°).

Figure 9. Dependence of the failure pattern on the slope inclination and the soil internal friction angle.

Figure 10. Stability number for slopes in the presence of seepage for slopes with inclination 30° to 90°: (a) $r_u = 0.25$ and narrow slopes, $B/L \leq 1.0$, (b) $r_u = 0.25$ and slopes, $B/L \geq 1.5$, (c) $r_u = 0.5$ and narrow slopes, $B/L \leq 1.0$, and (d) $r_u = 0.5$ and wide slopes, $B/L \geq 1.5$

Figure 11. Stability number for slopes subjected to horizontal acceleration: (a) $k_h = 0.1$ and narrow slopes, $B/L \leq 1.0$, (b) $k_h = 0.1$ and wide slopes, $B/L \geq 1.5$, (c) $k_h = 0.2$ and narrow slopes, $B/L \leq 1.0$, (d) $k_h = 0.2$ and wide slopes, $B/L \geq 1.5$, (e) $k_h = 0.3$ and narrow slopes, $B/L \leq 1.0$, and (f) $k_h = 0.3$ and wide slopes, $B/L \geq 1.5$.

Figure 12. Comparison of calculated stability numbers to those in [17] for slopes of different widths.

Figure 13. Comparison of calculated stability numbers to those in [19] for selected seepage and seismic acceleration, for $B/H = 1.5$.

Figure 14. Explanation of the impact of geometrical limitations on the outcome of the analysis.

Figure 15. (a) The shape of a failure surface with limitation $r' = 0$, and (b) failure surface allowing $r' > 0$, and also permitting the center line (dashed) to intersect the slope.